行政院國家科學委員會專題研究計畫 成果報告

旋轉彎曲圓盤之挫曲理論與實驗(2/2)
研究成果報告(完整版)

計 畫 類 別 ：個別型
計 畫 編 號 ：NSC 95-2221-E-002-226-
執 行 期 間 ：95 年 08 月 01 日至 96 年 07 月 31 日
執 行 單 位 ：國立臺灣大學機械工程學系暨研究所

計 畫 主 持 人：陳振山

計畫參與人員：碩士班研究生-兼任助理：盧志豪、林勇志、李志章
臨時工：廖慶彰

處 理 方 式 ：本計畫可公開查詢

中 華 民 國 96 年 09 月 20 日

旋轉彎曲圓盤之挫曲理論與實驗(2/2)

Experiment and Theory on the Snap-Through Buckling of a Spinning Non-Flat Disk

計畫編號: NSC 95-2212-E-002-012

執行期限: 95年8月1日至96年7月31日

計畫主持人: 陳振山 jschen@ntu.edu.tw

執行機關: 國立台灣大學機械系

報告目錄

註:本報告內容已投稿 International Journal of Nonlinear Mechanics, 並於2007年5月21日被接受

摘要

本計劃接續前一年的工作，探討非對稱彎曲旋轉圓盤的穩態變形與反挫曲現象。圓盤的初始形狀與變形均由軸對稱與非對稱模態所組成。若軸對稱圓盤加入一個節徑的非對稱模態，則輕微的增加反挫曲臨界轉速。反之，若加入兩個節徑以上的非對稱模態，則顯著降低反挫曲臨界轉速。實驗以非對稱彎曲的紅銅片為樣本，其中初始形狀由軸對稱與兩個節徑的非對稱模態所組成。實驗量測結果可驗證理論的預測

關鍵詞：旋轉彎曲圓盤；馮卡門平板模型；跳躍式挫曲

Abstract

In this project we extend the analysis on the spinning non-flat disk to the case when both the initial and the deformed shapes of the disk are allowed to have axisymmetrical and unsymmetrical components. Attention is focused on the effect of the unsymmetrical component on the overall deformation and stability of the spinning disk. It is found that the unsymmetrical component with one nodal-diameter tends to slightly defer the occurrence of the reverse snapping phenomenon. On the other hand, all other unsymmetrical components with more than one nodal-diameter tend to reduce dramatically the reverse snapping speed. Experiment is conducted on a non-flat brass disk containing an axisymmetrical component and an unsymmetrical component with two nodal diameters. The experimental measurement confirms the theoretical prediction.

Keywords: spinning non-flat disk; von Karman plate model; snap-through buckling

1. **Introduction**

Most of the researches in flexible disk dynamics [1] assume that the disk is perfectly flat before deformation. However, it is inevitable that runout be produced in the manufacturing process of a disk. In investigating the head-disk interface of a floppy disk drive, Ono and Maeno [2] concluded that it is necessary to take into account the non-flatness of the disk in order to model the interface force correctly. Carpino [3] studied the interaction between the gas flow and a disk of initial transverse runout rotating close to a rigid flat plate. To study the effect of spinning on the disk runout, Benson and Cole [4] analyzed four example warped disks, and conducted experiment on one of them. They found that disk runout tends to be flattened as the rotation speed increases. Jia [5] used Galerkin's method to solve the similar problem with emphasis on the disk deformation when the rotation speed is high. In these studies the runout and the deformation of the disks are assumed to be of the same order of magnitude as the thickness, and linearized plate equation is used to predict the steady state deflection.

Recently, Chen and Lin [6] extended Benson and Cole's [4] work to consider the steady state deflection and stability of a spinning disk with moderately large axisymmetrical warpage. Non-linear von Karman's plate model is adopted to formulate the governing equations. They reported that when the initial height of the axisymmetrical warpage is sufficiently large, there can exist more than one stable equilibrium position. Both theoretical and experimental investigations indicate that if the disk is initially in the unstressed position, centrifugal force only flattens the non-flat disk and the disk is always on the same side of the base plane no matter how high the rotation speed is. On the other hand, if the non-flat disk is initially in the stressed position, it will be snapped to the other side when the rotation speed reaches a critical value. This one-way snapping phenomenon may be called "reverse snapping." Recently, Chen and Huang [7] demonstrated a similar reverse snapping phenomenon when a full shallow shell is loaded by uniform in-plane tension on the outer rim. The loading mechanism in [7] is different from the one in [6].

There are several questions remained unanswered in Chen and Lin's paper [6]. First of all, for a non-flat disk with axisymmetrical initial shape, there is no guarantee that

the steady state deformations are also axisymmetrical. Previous experience in shallow shell theory [8] indicates that by including unsymmetrical assumed modes in the solution, the critical load of an axisymmetrical shell under axisymmetrical loading is dramatically reduced compared to the critical load predicted via a purely axisymmetrical theory. In other words, the snap-through phenomenon in an axisymmetrical shallow shell is inherently unsymmetrical, in spite of the fact that the lateral load is also axisymmetrical. It remains to be seen whether this is the case in a spinning axisymmetrical disk.

In the experiments conducted by Chen and Lin [6], they prepared a series of disks with axisymmetrical warpages. However, unwanted circumferential waviness always exists in the manufactured specimens. They reported that when the initial shape of the disk is close to axisymmetrical, the experimentally observed snapping speed agrees very well with the theoretical prediction. On the other hand, when the wavy amplitude on the outer rim amounts to about 30% of the mean height, the reverse snapping speed observed in the experiment is lower than the theoretical prediction by the order of about 25%. In light of these observations, the second question remained to be answered is how the unsymmetrical component of the initial shape affects the overall deformation and the reverse snapping speed. To answer this question, we need to extend Chen and Lin's axisymmetrical disk to a non-flat disk with a dominant axisymmetrical component and a smaller unsymmetrical component. This investigation may find practical application in circular saw cutting. In sawmills, a newly installed saw blade is almost perfectly flat. After several working hours, however, the saw blade becomes warped and is in need of leveling regularly [9]. Before tackling the problem of a spinning warped disk under cutting force, it is desirable to first understand how the warped disk deforms when it rotates freely. In general the warped saw blade is of unsymmetrical shape.

2. Equations of Motion

From the theory explained in [6], it follows that the equations of motion of a spinning non-flat disk, in terms of transverse displacement $w(r,\theta,t)$ and stress function $\phi(r,\theta,t)$ can be written as,

$$\rho h w_{,tt} + D\nabla^4(w - w_0) = w_{,rr}\left(r^{-1}\phi_{,r} + r^{-2}\phi_{,\theta\theta}\right) +$$
$$\left(r^{-1}w_{,r} + r^{-2}w_{,\theta\theta}\right)\phi_{,rr} - 2\left(r^{-1}w_{,\theta}\right)_{,r}\left(r^{-1}\phi_{,\theta}\right)_{,r} - \rho h\Omega^2 r\left(\frac{r}{2}\nabla^2 w + w_{,r}\right) \quad (1)$$

$$\nabla^4\phi = Eh\Big[-w_{,rr}\left(r^{-1}w_{,r} + r^{-2}w_{,\theta\theta}\right) + \left(r^{-1}w_{,r\theta} - r^{-2}w_{,\theta}\right)^2$$
$$+ w_{0,rr}\left(r^{-1}w_{0,r} + r^{-2}w_{0,\theta\theta}\right) - \left(r^{-1}w_{0,r\theta} - r^{-2}w_{0,\theta}\right)^2\Big] + 2(1-\nu)\rho h\Omega^2 \quad (2)$$

$w_0(r,\theta)$ is the initial shape of the disk. Both w and w_0 are measured from the same base plane, as shown in Fig. 1. (r,θ) are polar coordinates relative to a disk-fixed frame. Ω is the constant rotation speed. The parameters ρ, E, ν, and D are the mass density, Young's modulus, Poisson ratio, and flexural rigidity of the disk, respectively. In Eqs. (1) and (2) von Karman's plate model taking into account the membrane stretching due to bending deflection is adopted. In Eq. (2) we ignore the in-plane inertia of the spinning disk. In the special case when w_0=0, Eqs. (1) and (2) reduce to the nonlinear equations of motion of a spinning flat disk formulated by Nowinski [10].

Stress function ϕ in Eqs. (1) and (2) is related to the membrane stress resultants N_r, N_θ, and $N_{r\theta}$ by,

$$N_r = r^{-1}\phi_{,r} + r^{-2}\phi_{,\theta\theta} - \frac{1}{2}\rho h\Omega^2 r^2 \quad (3)$$

$$N_\theta = \phi_{,rr} - \frac{1}{2}\rho h\Omega^2 r^2 \quad (4)$$

$$N_{r\theta} = -\left(r^{-1}\phi_{,\theta}\right)_{,r} \quad (5)$$

The material of the disk is assumed to obey Hooke's law and the relations between the stress resultants and the in-plane strains are

$$\varepsilon_r = \frac{1}{hE}\left(N_r - \nu N_\theta\right) \quad (6)$$

$$\varepsilon_\theta = \frac{1}{hE}\left(N_\theta - \nu N_r\right) \quad (7)$$

$$\gamma_{r\theta} = \frac{2(1+\nu)}{hE}N_{r\theta} \quad (8)$$

The relations between the strains and the displacements are nonlinear,

$$\varepsilon_r = u_{r,r} + \frac{1}{2}\left(w_{,r}\right)^2 - \frac{1}{2}\left(w_{0,r}\right)^2 \quad (9)$$

$$\varepsilon_\theta = r^{-1}u_r + r^{-1}u_{\theta,\theta} + \frac{1}{2}r^{-2}\left(w_{,\theta}\right)^2 - \frac{1}{2}r^{-2}\left(w_{0,\theta}\right)^2 \quad (10)$$

$$\gamma_{r\theta} = \left[r^{-1}u_{r,\theta} + u_{\theta,r} - r^{-1}u_\theta + r^{-1}w_{,r}w_{,\theta} - r^{-1}w_{0,r}w_{0,\theta}\right] \quad (11)$$

where u_r and u_θ are the radial and tangential displacements of a material point relative to the body-fixed coordinate system.

We define the displacement field u as

$$u = w - w_0 \tag{12}$$

The above equations can be non-dimensionalized by introducing the following dimensionless quantities,

$$t^* = \frac{t}{b^2}\sqrt{\frac{D}{\rho h}},\quad \Omega^* = \Omega b^2\sqrt{\frac{\rho h}{D}},\quad r^* = \frac{r}{b},\quad (u^*, w^*, w_0^*) = \frac{1}{h}(u, w, w_0),$$
$$\phi^* = \frac{\phi}{D},\quad \eta = \frac{a}{b},\quad \left(N_r^*, N_\theta^*, N_{r\theta}^*\right) = \frac{b^2}{D}\left(N_r, N_\theta, N_{r\theta}\right) \tag{13}$$

After substituting Eq. (12) into Eqs. (1) and (2), nondimensionalizing them, and dropping the superposed asterisks thereafter for simplicity, we can re-write the equations of motion in the dimensionless forms,

$$\begin{aligned} u_{,tt} + \nabla^4 u = {} & \left(u + w_0\right)_{,rr}\left(r^{-1}\phi_{,r} + r^{-2}\phi_{,\theta\theta}\right) + \left[r^{-1}\left(u + w_0\right)_{,r} + r^{-2}\left(u + w_0\right)_{,\theta\theta}\right]\phi_{,rr} \\ & - 2\left[r^{-1}\left(u + w_0\right)_{,\theta}\right]_{,r}\left(r^{-1}\phi_{,\theta}\right)_{,r} - \Omega^2 r\left[\frac{r}{2}\nabla^2\left(u + w_0\right) + \left(u + w_0\right)_{,r}\right] \end{aligned} \tag{14}$$

$$\begin{aligned} \nabla^4\phi = {} & 12\left(1 - \nu^2\right)\Big[-u_{,rr}\left(r^{-1}u_{,r} + r^{-2}u_{,\theta\theta}\right) + \left(r^{-1}u_{,r\theta} - r^{-2}u_{,\theta}\right)^2 \\ & + 2\left(r^{-1}u_{,r\theta} - r^{-2}u_{,\theta}\right)\left(r^{-1}w_{0,r\theta} - r^{-2}w_{0,\theta}\right) \\ & - w_{0,rr}\left(r^{-1}u_{,r} + r^{-2}u_{,\theta\theta}\right) - u_{,rr}\left(r^{-1}w_{0,r} + r^{-2}w_{0,\theta\theta}\right)\Big] + 2(1 - \nu)\Omega^2 \end{aligned} \tag{15}$$

The disk is fully clamped at the inner radius $r = \eta$ and is free at the outer radius r=1. The boundary conditions for u at $r = \eta$ are

$$u = 0 \tag{16}$$
$$u_{,r} = 0 \tag{17}$$

At r=1, both the shear force and bending moment are zero,

$$\left(\nabla^2 u\right)_{,r} + r^{-2}(1 - \nu)\left(u_{,r\theta\theta} - r^{-1}u_{,\theta\theta}\right) = 0 \tag{18}$$
$$u_{,rr} + \nu r^{-1}\left(u_{,r} + r^{-1}u_{,\theta\theta}\right) = 0 \tag{19}$$

The zero in-plane displacement boundary conditions for ϕ at $r = \eta$ can be written as

$$\phi_{,rr} - \nu r^{-1}\phi_{,r} - \nu r^{-2}\phi_{,\theta\theta} = \frac{1 - \nu}{2}\Omega^2\eta^2 \tag{20}$$
$$r\phi_{,rrr} + (\nu - 1)r^{-1}\phi_{,r} + (\nu + 2)r^{-1}\phi_{,r\theta\theta} - 3r^{-2}\phi_{,\theta\theta} = \frac{1 - \nu}{2}\Omega^2\eta^2 \tag{21}$$

The derivation of Eqs. (20) and (21) can be found in Appendix. The traction-free boundary conditions N_r=0 and $N_{r\theta}$=0 at r=1 can be written as,

$$r^{-1}\phi_{,r} + r^{-2}\phi_{,\theta\theta} = \frac{1}{2}\Omega^2 \tag{22}$$

$$\left(r^{-1}\phi_{,\theta}\right)_{,r} = 0 \tag{23}$$

It is noted that while Eqs. (14) and (15) are nonlinear in terms of u, they are linear in ϕ. Therefore we can divide the stress function ϕ in Eq. (15) into two parts,

$$\phi = \phi_1 + \phi_2 . \tag{24}$$

The first part ϕ_1 accounts for the centrifugal effect, and satisfies the inhomogeneous equation

$$\nabla^4\phi_1 = 2(1-\nu)\Omega^2 \tag{25}$$

and the same inhomogeneous boundary conditions as ϕ does, i.e., Eqs. (20)-(23). The second part ϕ_2 satisfies the equation,

$$\begin{aligned}\nabla^4\phi_2 = 12\left(1-\nu^2\right)\Big[&-u_{,rr}\left(r^{-1}u_{,r} + r^{-2}u_{,\theta\theta}\right) + \left(r^{-1}u_{,r\theta} - r^{-2}u_{,\theta}\right)^2 \\ &+ 2\left(r^{-1}u_{,r\theta} - r^{-2}u_{,\theta}\right)\left(r^{-1}w_{0,r\theta} - r^{-2}w_{0,\theta}\right) \\ &- w_{0,rr}\left(r^{-1}u_{,r} + r^{-2}u_{,\theta\theta}\right) - u_{,rr}\left(r^{-1}w_{0,r} + r^{-2}w_{0,\theta\theta}\right)\Big]\end{aligned} \tag{26}$$

and the homogeneous version of boundary conditions (20)-(23). After solving ϕ_1 and substituting it into the dimensionless forms of Eqs. (3) and (4) (replacing ϕ by ϕ_1), we can derive the axisymmetrical stress resultants $\Omega^2\overline{N}_{1r}$ and $\Omega^2\overline{N}_{1\theta}$ due to centrifugal effect. Functions $\overline{N}_{1r}$ and $\overline{N}_{1\theta}$ can be calculated as

$$\overline{N}_{1r} = C_1 + C_2 r^{-2} + C_3 r^2 \tag{27}$$

$$\overline{N}_{1\theta} = C_1 - C_2 r^{-2} + C_4 r^2 \tag{28}$$

where

$$C_1 = \frac{(1+\nu)}{8}\frac{(\nu-1)\eta^4 - (3+\nu)}{(\nu-1)\eta^2 - (1+\nu)},\ C_2 = \frac{(1-\nu)\eta^2}{8}\frac{(\nu+1)\eta^2 - (3+\nu)}{(\nu-1)\eta^2 - (1+\nu)}$$

$$C_3 = -\frac{(3+\nu)}{8}\ ,\ C_4 = -\frac{(1+3\nu)}{8}$$

After substituting Eq. (24) into Eq. (14) we can re-write the equation for u as

$$u_{,tt} + \nabla^4 u - \Omega^2 r^{-1}\left[\overline{N}_{1r} r (u+w_0)_{,r}\right]_{,r} - \Omega^2 r^{-2}\overline{N}_{1\theta}(u+w_0)_{,\theta\theta} =$$

$$(u+w_0)_{,rr}\left(r^{-1}\phi_{2,r} + r^{-2}\phi_{2,\theta\theta}\right) + \left[r^{-1}(u+w_0)_{,r} + r^{-2}(u+w_0)_{,\theta\theta}\right]\phi_{2,rr}$$

$$-2\left[r^{-1}\left(u+w_0\right)_{,\theta}\right]_{,r}\left(r^{-1}\phi_{2,\theta}\right)_{,r} \tag{29}$$

The problem now boils down to solving Eqs. (26) and (29) subject to the homogeneous version of boundary conditions (16) to (23), i.e., by imposing $\Omega^2 = 0$ in boundary conditions (16)-(23).

3. Discretization

In order to solve the coupled nonlinear equations (26) and (29), we use the Galerkin method by assuming that the displacement u and stress function ϕ_2 can be expanded in terms of assumed modes u_{mn} and ϕ_{mn} as following,

$$\phi_2(r,\theta,t) = \sum_{m=0}^{\infty}\sum_{n=0}^{\infty}\left[d_{mn(c)}(t)\phi_{mn(c)}(r,\theta) + d_{mn(s)}(t)\phi_{mn(s)}(r,\theta)\right] \tag{30}$$

$$u(r,\theta,t) = \sum_{m=0}^{\infty}\sum_{n=0}^{\infty}\left[c_{mn(c)}(t)u_{mn(c)}(r,\theta) + c_{mn(s)}(t)u_{mn(s)}(r,\theta)\right] \tag{31}$$

$c_{mn(c)}(t)$, $c_{mn(s)}(t)$, $d_{mn(c)}(t)$, $d_{mn(s)}(t)$ are real functions of time. $u_{mn(c)}$, $u_{mn(s)}$, $\phi_{mn(c)}$, and $\phi_{mn(s)}$ satisfy the equations

$$\nabla^4 u_{mn} - \alpha_{mn}^4 u_{mn} = 0 \tag{32}$$

$$\nabla^4 \phi_{mn} - \beta_{mn}^4 \phi_{mn} = 0 \tag{33}$$

and the same homogeneous boundary conditions as u and ϕ_2 do. The subscripts "(c)" and "(s)" represent cosine and sine modes. Subscripts m and n represent the number of nodal circles and nodal diameters, respectively. It is noted that $u_{mn(c)}$ and $u_{mn(s)}$ are the bending vibration mode shapes of a flat disk. On the other hand, $\phi_{mn(c)}$, and $\phi_{mn(s)}$ have no specific physical meaning. Instead, they are adopted simply as mathematical tools which are eigenfunctions of a self-adjoint system. It can be proved mathematically and verified numerically that $u_{mn(c)}$ and $u_{mn(s)}$ form an orthonormal set, while $\phi_{mn(c)}$, and $\phi_{mn(s)}$ form another orthonormal set. $u_{mn(c)}$, $u_{mn(s)}$, $\phi_{mn(c)}$, and $\phi_{mn(s)}$ can be expressed in the following forms,

$$u_{mn(c)}(r,\theta) = R_{mn}(r)\cos n\theta \quad , \quad u_{mn(s)}(r,\theta) = R_{mn}(r)\sin n\theta \tag{34}$$

$$\phi_{mn(c)}(r,\theta) = S_{mn}(r)\cos n\theta \quad , \quad \phi_{mn(s)}(r,\theta) = S_{mn}(r)\sin n\theta \tag{35}$$

$R_{mn}(r)$ and $S_{mn}(r)$ are the radial components of functions u_{mn} and ϕ_{mn}. It is noted that the assumed functions $u_{mn(c)}$, $u_{mn(s)}$, $\phi_{mn(c)}$, and $\phi_{mn(s)}$ satisfy the same homogeneous

boundary conditions as u and ϕ_2 do. Therefore, u and ϕ_2 in Eqs. (30) and (31) satisfy the associated boundary conditions automatically.

For the sake of faster convergence, we choose the initial shape w_0 to be the combination of assumed modes $u_{mn(c)}$, i.e.,

$$w_0 = \sum_{i=0}^{N} H_i \overline{w}_i \tag{36}$$

where

$$\overline{w}_i = \frac{u_{0i(c)}}{u_{0i(c)}\Big|_{r=1,\theta=0}} \tag{37}$$

H_i represent the heights at the point (r=1, θ=0) of various components of the initial shape. In Eq. (36) we assume that the initial shape consists of only the cosine modes. For more general case with w_0 containing both the cosine and sine modes the formulation is similar, only more complicated. After substituting Eqs. (30), (31), and (36) into Eq. (26), multiplying both sides by $\phi_{pq(c)}$ and $\phi_{pq(s)}$, respectively, and integrating, we obtain the expressions of $d_{pq}^{(c)}$ and $d_{pq}^{(s)}$ as,

$$d_{pq}^{(c)} = \sum_{k=0}^{\infty}\sum_{s=0}^{\infty}\left\{\sum_{i=0}^{\infty} c_{ks(c)} H_i \Psi_{pqksi}^{(c)} + \sum_{l=0}^{\infty}\sum_{j=0}^{\infty}\left[c_{ks(c)}c_{lj(c)}\Psi_{pqkslj}^{(c)(1)} + c_{ks(s)}c_{lj(s)}\Psi_{pqkslj}^{(c)(2)}\right]\right\} \tag{38}$$

$$d_{pq}^{(s)} = \sum_{k=0}^{\infty}\sum_{s=0}^{\infty}\left\{\sum_{i=0}^{\infty} c_{ks(c)} H_i \Psi_{pqksi}^{(s)} + \sum_{l=0}^{\infty}\sum_{j=0}^{\infty}\left[c_{ks(c)}c_{lj(c)}\Psi_{pqkslj}^{(s)(1)} + c_{ks(s)}c_{lj(s)}\Psi_{pqkslj}^{(s)(2)}\right]\right\} \tag{39}$$

After substituting Eqs. (38), (39), (30), and (31) into Eq. (29), multiplying by $u_{mn(c)}$ and $u_{mn(s)}$, respectively, and integrating, we then obtain

$$\begin{aligned}
&\ddot{c}_{mn(c)} + \alpha_{mn}^4 c_{mn(c)} - \Omega^2 \sum_{i=0}^{\infty} H_i \Lambda_{mni}^{(c)} - \Omega^2 \sum_{f=0}^{\infty}\sum_{g=0}^{\infty} c_{fg(c)} \Lambda_{mnfg}^{(c)} \\
&= \sum_{p=0}^{\infty}\sum_{q=0}^{\infty}\sum_{k=0}^{\infty}\sum_{s=0}^{\infty}\left\{\left[\sum_{i=0}^{\infty} c_{ks(c)} H_i \Psi_{pqksi}^{(c)} + \sum_{l=0}^{\infty}\sum_{j=0}^{\infty}\left(c_{ks(c)}c_{lj(c)}\Psi_{pqkslj}^{(c)(1)} + c_{ks(s)}c_{lj(s)}\Psi_{pqkslj}^{(c)(2)}\right)\right]\right. \\
&\qquad \left.\left[\sum_{f=0}^{\infty}\sum_{g=0}^{\infty} c_{fg(c)} \Lambda_{mnfgpq}^{(c)(c)} + \sum_{i=0}^{\infty} H_i \Lambda_{mnpqi}^{(c)(c)}\right]\right\} \\
&+ \sum_{p=0}^{\infty}\sum_{q=0}^{\infty}\sum_{k=0}^{\infty}\sum_{s=0}^{\infty}\left\{\left[\sum_{i=0}^{\infty} c_{ks(s)} H_i \Psi_{pqksi}^{(s)} + \sum_{l=0}^{\infty}\sum_{j=0}^{\infty}\left(c_{ks(c)}c_{lj(s)}\Psi_{pqkslj}^{(s)(1)} + c_{ks(s)}c_{lj(c)}\Psi_{pqkslj}^{(s)(2)}\right)\right]\right. \\
&\qquad \left.\left(\sum_{f=0}^{\infty}\sum_{g=0}^{\infty} c_{fg(s)} \Lambda_{mnfgpq}^{(c)(s)}\right)\right\}
\end{aligned} \tag{40}$$

$$\ddot{c}_{mn(s)} + \alpha_{mn}^4 c_{mn(s)} - \Omega^2 \sum_{f=0}^{\infty}\sum_{g=0}^{\infty} c_{fg(s)} \Lambda_{mnfg}^{(s)}$$

$$= \sum_{p=0}^{\infty}\sum_{q=0}^{\infty}\sum_{k=0}^{\infty}\sum_{s=0}^{\infty}\left\{\left[\sum_{i=0}^{\infty} c_{ks(c)} H_i \Psi^{(c)}_{pqksi} + \sum_{l=0}^{\infty}\sum_{j=0}^{\infty}\left(c_{ks(c)}c_{lj(c)}\Psi^{(c)(1)}_{pqkslj} + c_{ks(s)}c_{lj(s)}\Psi^{(c)(2)}_{pqkslj}\right)\right]\right.$$
$$\left.\left(\sum_{f=0}^{\infty}\sum_{g=0}^{\infty} c_{fg(s)}\Lambda^{(s)(c)}_{mnfgpq}\right)\right\}$$
$$+ \sum_{p=0}^{\infty}\sum_{q=0}^{\infty}\sum_{k=0}^{\infty}\sum_{s=0}^{\infty}\left\{\left[\sum_{i=0}^{\infty} c_{ks(s)} H_i \Psi^{(s)}_{pqksi} + \sum_{l=0}^{\infty}\sum_{j=0}^{\infty}\left(c_{ks(c)}c_{lj(s)}\Psi^{(s)(1)}_{pqkslj} + c_{ks(s)}c_{lj(c)}\Psi^{(s)(2)}_{pqkslj}\right)\right]\right.$$
$$\left.\left[\sum_{f=0}^{\infty}\sum_{g=0}^{\infty} c_{fg(c)}\Lambda^{(s)(s)}_{mnfgpq} + \sum_{i=0}^{\infty} H_i \Lambda^{(s)(s)}_{mnpqi}\right]\right\} \qquad (41)$$

The constants involved in Eqs. (38) to (41) are listed in the following,

$$\Psi^{(c)}_{pqksi} = A_1\gamma^{(1)}_{qsi} - A_2\gamma^{(2)}_{siq} \quad , \quad \Psi^{(s)}_{pqksi} = A_1\gamma^{(2)}_{qsi} + A_2\gamma^{(2)}_{qis}$$
$$\Psi^{(c)(1)}_{pqkslj} = A_3\gamma^{(1)}_{qsj} + A_4\gamma^{(2)}_{sjq} \quad , \quad \Psi^{(c)(2)}_{pqkslj} = A_3\gamma^{(2)}_{sjq} + A_4\gamma^{(1)}_{qsj}$$
$$\Psi^{(s)(1)}_{pqkslj} = A_3\gamma^{(2)}_{qjs} - A_4\gamma^{(2)}_{qsj} \quad , \quad \Psi^{(s)(2)}_{pqkslj} = A_3\gamma^{(2)}_{qsj} - A_4\gamma^{(2)}_{qjs}$$
$$\Lambda^{(c)(c)}_{mnfgpq} = A_5\gamma^{(1)}_{ngq} - A_6\gamma^{(2)}_{gqn} \quad , \quad \Lambda^{(c)(s)}_{mnfgpq} = A_5\gamma^{(2)}_{gqn} - A_6\gamma^{(1)}_{ngq}$$
$$\Lambda^{(s)(c)}_{mnfgpq} = A_5\gamma^{(2)}_{ngq} + A_6\gamma^{(2)}_{nqg} \quad , \quad \Lambda^{(s)(s)}_{mnfgpq} = A_5\gamma^{(2)}_{nqg} + A_6\gamma^{(2)}_{ngq}$$
$$\Lambda^{(c)(c)}_{mnpqi} = A_7\gamma^{(1)}_{nqi} - A_8\gamma^{(2)}_{qin} \quad , \quad \Lambda^{(s)(s)}_{mnpqi} = A_7\gamma^{(2)}_{nqi} + A_8\gamma^{(2)}_{niq}$$
$$\Lambda^{(c)}_{mni} = A_9\chi^{(1)}_{ni} \quad , \quad \Lambda^{(c)}_{mnfg} = A_{10}\chi^{(1)}_{ng} \quad , \quad \Lambda^{(s)}_{mnfg} = A_{10}\chi^{(2)}_{ng}$$

where

$$\gamma^{(1)}_{lmn} = \int_{\theta=0}^{2\pi}\cos(l\theta)\cos(m\theta)\cos(n\theta)d\theta\,, \qquad \gamma^{(2)}_{lmn} = \int_{\theta=0}^{2\pi}\sin(l\theta)\sin(m\theta)\cos(n\theta)d\theta$$

$$\chi^{(1)}_{mn} = \begin{cases} 2\pi & ,when\ m=n=0 \\ \pi & ,when\ m=n\neq 0 \\ 0 & ,when\ m\neq n \end{cases} \qquad \chi^{(2)}_{mn} = \begin{cases} 0 & ,when\ m=n=0 \\ \pi & ,when\ m=n\neq 0 \\ 0 & ,when\ m\neq n \end{cases}$$

$$A_1 = -\frac{12(1-\nu^2)}{\beta^4_{pq}}\int_{r=\eta}^{1} S_{pq}\left[\overline{w}_{i,rr}\left(r^{-1}R_{ks,r} - r^{-2}s^2R_{ks}\right) + R_{ks,rr}\left(r^{-1}\overline{w}_{i,r} - r^{-2}i^2\overline{w}_i\right)\right]rdr$$

$$A_2 = -\frac{12(1-\nu^2)}{\beta^4_{pq}}\int_{r=\eta}^{1} S_{pq}\left[2\left(r^{-1}sR_{ks,r} - r^{-2}sR_{ks}\right)\left(r^{-1}i\overline{w}_{i,r} - r^{-2}i\overline{w}_i\right)\right]rdr$$

$$A_3 = -\frac{12(1-\nu^2)}{\beta^4_{pq}}\int_{r=\eta}^{1} S_{pq}R_{ks,rr}\left(r^{-1}R_{lj,r} - r^{-2}j^2R_{lj}\right)rdr$$

$$A_4 = -\frac{12(1-\nu^2)}{\beta^4_{pq}}\int_{r=\eta}^{1} S_{pq}\left(2r^{-3}sjR_{ks,r}R_{lj} - r^{-2}sjR_{ks,r}R_{lj,r} - r^{-4}sjR_{ks}R_{lj}\right)rdr$$

$$A_5 = \int_{r=\eta}^{1} R_{mn}\left[R_{fg,rr}\left(r^{-1}S_{pq,r} - r^{-2}q^2S_{pq}\right) + S_{pq,rr}\left(r^{-1}R_{fg,r} - r^{-2}g^2R_{fg}\right)\right]rdr$$

$$A_6 = \int_{r=\eta}^{1} R_{mn}\left[2gq\left(r^{-1}R_{fg}\right)_{,r}\left(r^{-1}S_{pq}\right)_{,r}\right]rdr$$

$$A_7 = \int_{r=\eta}^{1} R_{mn}\left[\overline{w}_{i,rr}\left(r^{-1}S_{pq,r} - r^{-2}q^2 S_{pq}\right) + S_{pq,rr}\left(r^{-1}\overline{w}_{i,r} - r^{-2}i^2\overline{w}_i\right)\right]rdr$$

$$A_8 = \int_{r=\eta}^{1} R_{mn}\left[2\left(r^{-1}i\overline{w}_i\right)_{,r}\left(r^{-1}qS_{pq}\right)_{,r}\right]rdr$$

$$A_9 = \int_{r=\eta}^{1} R_{mn}\left[\overline{N}_{1r,r}\overline{w}_{i,r} + r^{-1}\overline{N}_{1r}\overline{w}_{i,r} + \overline{N}_{1r}\overline{w}_{i,rr} - r^{-2}i^2\overline{N}_{1\theta}\overline{w}_i\right]rdr$$

$$A_{10} = \int_{r=\eta}^{1} R_{mn}\left[\left(\overline{N}_{1r,r}R_{fg,r} + r^{-1}\overline{N}_{1r}R_{fg,r} + \overline{N}_{1r}R_{fg,rr}\right) - r^{-2}g^2\overline{N}_{1\theta}R_{fg}\right]rdr$$

In calculating the steady state solutions the time-derivative terms $\ddot{c}_{mn(c)}$ and $\ddot{c}_{mn(s)}$ in Eqs. (40) and (41) can be dropped. Newton-Raphson method is used to solve the nonlinear algebraic equations. In stability analysis, small perturbations are added to the steady state solutions and substituted back into Eqs. (40) and (41). After linearization, we can solve for the eigenvalues of the linearized homogeneous equations. If the real parts of any of the eigenvalues are positive, then the corresponding steady state solutions are unstable. In the special case when both the initial shape and the deformed shape are assumed to be axisymmetrical, these complicated equations reduce to the simplified version presented in [6].

4. Equilibrium Positions of a Spinning Axisymmetrical Disk

In studying the deformation of an axisymmetrical disk, Chen and Lin [6] used only axisymmetrical assumed modes in the solution expansion. It remains unanswered whether it is possible for the axisymmetrical disk to have unsymmetrical deformation, or whether the inclusion of the unsymmetrical assumed modes will affect the snapping speed prediction. In this section we focus on the effect of including the unsymmetrical assumed modes in the solution expansion. This result also serves as a reference for the analysis of the deformation of a disk which is initially unsymmetrical.

The need for such an analysis can be traced back to the development of the shallow shell theory. For an axisymmetrical shell clamped on the outer rim and loaded by uniform pressure, experimental measurement of the snap-through buckling load is found to be significantly smaller than the theoretical prediction based on axisymmetrical deformation. Huang [8] demonstrated that if the unsymmetrical assumed modes are included in the

solution expansion, the predicted buckling load will be smaller than the one based solely on axisymmetrical assumed modes. This phenomenon is more dramatic for shells with larger initial height. This discovery helps to partially close the gap between experiment and theory. Because the loading mechanism in the current paper is different from the one in the classical shell theory [8], it remains to be examined whether the unsymmetrical assumed modes will change the reverse snapping speed prediction of an axisymmetrical disk.

Figure 2 shows the disk position at (r=1, θ=0) as a function of the rotation speed for an axisymmetrical disk with H_0=5. In all the calculations presented in this paper the Poisson ratio is assumed to be 0.3. Two assumed modes with coefficients c_{00} and $c_{01(c)}$ are sufficient to produce convergent solutions in this case. In this paper solid and dashed lines represent stable and unstable solutions, respectively. We notice that in the case when the disk is not rotating, it appears to possess five solutions, as shown in Fig. 2. Table 1 lists the coordinates c_{mn} of these five solutions. The positions P_0^1, P_0^2, and P_0^3 are three axisymmetrical solutions. The subscript "0" in these positions indicates that the solutions contain only the assumed modes with zero nodal-diameter. The superscript denotes the sequence number of these solutions from top to bottom in Fig. 2. The positions P_0^1 and P_0^3 are stable while P_0^2 is unstable. If the disk is in position P_0^1 when Ω=0, it will be flattened smoothly as the rotation speed increases. On the other hand, if the disk is in position P_0^3 (under the base plane and stressed) when Ω=0, it will be snapped to position P_0^1 when the rotation speed reaches a critical value Ω=8.26.

The three axisymmetrical positions in Fig. 2 are exactly the same as those presented in [6]. In other words, the inclusion of the unsymmetrical mode ($c_{01(c)}$) does not affect the axisymmetrical solutions obtained through the purely axisymmetrical theory. However, the inclusion of the unsymmetrical mode appears to produce two additional solutions P_{01}^1 and P_{01}^{1*}. The subscript "01" indicates that these solutions contain mainly the assumed modes with zero and one nodal-diameter. Therefore, they are unsymmetrical deformations. These unsymmetrical solutions are unstable. By inspecting Table 1, we know that these two solutions are physically identical, only 180 degrees apart

circumferentially. This is the case even when the disk is rotating. Therefore, the same superscript "1" indicates that they are actually the same mode of deformation. The superscript "*" emphasizes that they are "mathematically" different. Special attention is paid to the intersection of the loci of P_{01}^{1*} and P_0^3. It is noted that the stability of these two positions do not change after they intersect. In other words, the unsymmetrical solutions do not affect the stability of the axisymmetrical solutions. Therefore, we can conclude that for the analysis of a rotating axisymmetrical disk there is no need to include the unsymmetrical assumed modes in the solution.

For an axisymmetrical shallow shell under axisymmetrical lateral loading [8], on the other hand, the intersection of the loci of a stable axisymmetrical position and an unstable unsymmetrical position results in the change of stability of the axisymmetrical position. In other words, both the axisymmetrical and unsymmetrical positions become unstable after their loci cross over. This is the reason why in classical shallow shell theory the critical lateral load predicted via unsymmetrical formulation is substantially smaller than the one predicted without including the unsymmetrical assumed mode. This scenario does not occur in the case of a spinning axisymmetrical disk.

If we use the two assumed modes with coefficients c_{00} and $c_{01(s)}$, the resulted solutions are exactly the same as the ones obtained by using c_{00} and $c_{01(c)}$. If three modes c_{00}, $c_{01(c)}$, and $c_{01(s)}$ are used in the expansion, only two of the three resulted equations are independent. Therefore, for the analysis of an axisymmetrical disk, we need only the axisymmetrical and the cosine modes.

Figure 3 shows the case when the axisymmetrical disk has an initial height H_0=7. In the case when the disk is not rotating, there are, mathematically, 11 solutions. However, among them only eight are physically different. Five of these eight physically different positions are axisymmetrical, denoted by P_0^1 to P_0^5 in Fig. 3. Besides these 5 solutions there are 3 more unsymmetrical solutions, denoted by P_{01}^1, P_{01}^2, and P_{02}^1. It is noted that each of these three positions appears in pair mathematically in Fig.3. In all these solutions only the axisymmetrical positions P_0^1 and P_0^5 are stable. By comparing Figs. 2 and 3 we

notice that more unsymmetrical solutions appear when the initial height increases. In particular, unsymmetrical deformation (P_{02}^{1}) with two nodal-diameters starts to show up.

5. Equilibrium Positions of a Spinning Unsymmetrical Disk

In this section we investigate the deformation and stability of a rotating disk with initial shape containing both the axisymmetrical component H_0 and an unsymmetrical component H_i. Figure 4 shows the disk position at (r=1, θ=0) as a function of the rotation speed for a disk with initial height parameters H_0=5 and H_1=3. In Fig. 4 we use 12 assumed modes in the expansions (30) and (31). In the case when Ω=0, there exist seven equilibrium positions. Table 2 lists the coordinates c_{mn} of these positions. All these solutions are both mathematically and physically different. Among them only two are stable, they are $P_{01_c}^{1}$ and $P_{01_c}^{4}$. These two stable positions have similar components as the initial shape, i.e., the axisymmetrical mode and the $\cos\theta$-mode. It is noted that the positions $P_{01_{cs}}^{1}$ and $P_{01_{cs}}^{2}$ are two different configurations but trace the same locus in Fig. 4. If we replace the ordinate of the graph with the disk position at r=1 and $\theta=\frac{\pi}{2}$, we will see two separate loci merging as Ω increases. The subscript "1_{cs}" in the position label $P_{01_{cs}}^{1}$ indicates that the solution contains the modes $\cos\theta$ and $\sin\theta$. It is noted that the inclusion of the unsymmetrical component $c_{01(c)}$ in the initial shape destroys the dependence of the resulted equations as described in the last section for an axisymmetrical disk. Therefore, for a complete solution we need to include both the cosine and sine modes in the expansion. However, the inclusion of the sine assumed modes only affects positions $P_{01_{cs}}^{1}$ and $P_{01_{cs}}^{2}$, which are unstable and relatively unimportant. Therefore, for practical purpose we can use only the cosine modes in the solution to simplify the calculation. This simplification is certainly not applicable in the case when the disk initial shape contains the sine components.

Although the inclusion of the unsymmetrical component in the initial shape complicates the overall solution with more unsymmetrical solutions, most of them are unstable. We focus our attention on the effect of the component H_1 on the mean

deformation of the two stable solutions and the reverse snapping speed, which are observable in the laboratory. In Fig. 5 we show the mean heights of positions $P^1_{01_c}$ and $P^4_{01_c}$ on the outer rim with thick lines. These two positions are on the opposite sides of the base plane. The black dot signifies the rotation speed at which reverse snapping occurs. Also plotted as thin lines for comparison are the loci of the two stable solutions for the disk with H_0=5 and H_1=0, i.e., P^1_0 and P^3_0 in Fig. 2. It appears that the initial shape component H_1 tends to oppose the flattening effect due to rotation. In addition, it raises the reverse snapping speed slightly.

We now study the disk with initial height parameters H_0 and H_2. Figure 6 shows the disk position as a function of the rotation speed for a disk with H_0=5 and H_2=3. In the case when $\Omega = 0$, there exist seven equilibrium positions mathematically, but only five of them are physically different. Again, only two of these positions are stable, they are $P^1_{02_c}$ and $P^3_{02_c}$. These two stable positions have similar components as the initial shape, i.e., the axisymmetrical mode and the $\cos 2\theta$-mode. Figure 7 shows the mean heights on the outer rim of these two stable solutions with thick lines. The disk positions of its axisymmetrical counterpart are presented with thin lines for comparison. It appears that the initial height parameter H_2 tends to enhance the flattening effect due to rotation. More importantly, it reduces the reverse snapping speed by about 50%.

The effect of other initial shape components, such as H_3 and H_4, on the disk deformation can be examined in the similar manner. Detailed numerical results can be found in [11]. It can be concluded that for a disk with H_0 and an H_i with $i \geq 2$, the unsymmetrical component H_i tends to enhance the flattening effect and reduce the snapping speed. Therefore, H_1 is the only unsymmetrical component which increases the snapping speed. Figure 8 shows the relation between the reverse snapping speed Ω_{cr} and various unsymmetrical components H_i with $i \geq 1$. The axisymmetrical component H_0 is fixed at 5. It is observed that the unsymmetrical components with more nodal diameters tend to have more dramatic effect in reducing the reverse snapping speed. When the unsymmetrical component is large enough, the stable position on the other side of the base

plane will cease to exist. For instance, in the case when H_0=5 and $H_2 \geq 3.33$ the initial unstressed position will be the only stable solution of the disk.

6. Measurement of Steady State Deflection

In order to verify the above theoretical predictions, we conduct an experiment on the deflection measurement of a rotating disk with unsymmetrical initial shape. The disk is made from a brass sheet with thickness 0.4 *mm*. The Young's modulus and mass density of the material are 103 *GPa* and 8864 kg/m^3, respectively. The inner and outer radii of the disk are designed to be 3.75 and 15 *cm*, respectively. The initial shape of the disk is designed to approximate the shape

$$w_0 = H_0 \overline{w}_0 + H_2 \overline{w}_2 \tag{42}$$

The ratio between H_0 and H_2 is designed to be 5:3. We first machine an unsymmetrical mold of the desired initial shape on an NC milling machine. The flat brass sheet is bent and locked in the mold. The mold together with the bent brass sheet is then put in an oven to heat to $250^\circ C$ for one hour to relieve the internal stresses. The unsymmetrical disks are then polished and mounted on a clamping device with clamping radius 3.75 *cm*. The deformation of the spinning disk can be measured with a non-contact photonic probe.

Figure 9 shows the initial shape measurement of the brass disk in the circumferential direction on the outer rim when the disk is not rotating. The symbol • represents the measured height relative to the clamping plane at various points on the outer rim for both the unstressed and stressed positions. For the measured shape of the unstressed position, we can use a least square method to determine the initial height parameters as H_0 =7.3 and H_2 =5.3. With these estimated parameters we can then calculate the shape of the stressed position on the other side of the base plane. The theoretically predicted shapes in the circumferential direction of these two positions are plotted as solid lines in Fig. 9. It appears that the theory predicts the mean height of the stressed position quite well. However, the measured wavy amplitude of the stressed position is larger than the theoretical prediction. For convenient reference, we present the

measured results with both the dimensionless parameters (left and bottom sides) and the physical ones (right and top sides). The same labeling style is adopted in Fig. 10 as well.

The brass disk is then mounted on a motor. The rotation speed of the motor is varied at an increment of 90 *rpm*. The photonic probe used to measure the deflection of the disk is fixed in space. When the disk is in its initial unstressed position, the mean height variation due to rotation is marked with symbol Δ. The experiment stops at 1980 rpm. In another test we start the disk in the stressed position and increase the rotation speed. The mean height variation is marked with symbol $\times$. With more refined rotation speed increment, the disk is observed to snap to the other side when Ω reaches 9.6 (1675 rpm). The arrows in the figure indicate the direction of rotation speed variation in both tests.

The thick lines in Fig. 10 are the theoretical predictions of the two stable solutions based on the estimated parameters H_0=7.3 and H_2=5.3. We found that the measured deflections agree with the theoretical predictions reasonably well in both the upper and lower branches. The unsymmetrical theory predicts that snapping occurs at $\Omega = 10.1$ (1769 rpm). Therefore, the actual snapping speed is about 6% lower than the theoretical value. In Fig. 10 we also present the calculated results based on the axisymmetrical theory [6] as thin lines, which predicts that the disk snaps at $\Omega = 16.6$ (2908 rpm). It overestimates the snapping speed by about 40%. This experimental observation confirms our theoretical prediction, which states that the unsymmetrical component H_i with $i \geq 2$ tends to reduce the reverse snapping speed.

7. Conclusions

In this paper we study the steady state deflection of a spinning non-flat disk, both theoretically and experimentally. The initial and the deformed shapes of the non-flat disk are assumed to contain both axisymmetrical and unsymmetrical components. Von Karman's plate model taking into account the membrane stretching due to bending deflection is adopted to formulate the equations of motion. Galerkin's method is used to discrtetize the differential equations of motion. Several conclusions regarding the steady

state deflection and the reverse snapping speed of the spinning non-flat disk can be summarized in the following.

(1) In the case of an axisymmetrical disk, the inclusion of the unsymmetrical assumed modes in the solution expansion will not change the theoretical prediction on the stable configurations and the reverse snapping speed obtained with only axisymmetrical assumed modes. All the unsymmetrical deformations are unstable. Therefore, for the analysis of an axisymmetrical disk, the axisymmetrical theory as the one presented in [6] is sufficient.

(2) When a small unsymmetrical component is added onto the originally axisymmetrical initial shape, it tends to affect the mean height variation and the reverse snapping speed of the disk. The effect of an unsymmetrical component with one nodal-diameter is to increase the reverse snapping speed slightly. On the other hand, all the unsymmetrical components with more than one nodal-diameter tend to enhance the flattening effect due to rotation and to reduce dramatically the reverse snapping speed.

(3) Experiment is conducted on a non-flat brass disk containing an axisymmetrical component and a smaller unsymmetrical mode with two nodal-diameters. The experimental measurement on the mean deformation and the snapping speed of the spinning disk confirms the theoretical predictions.

References

[1] C.D. Mote, R. Szymani, A review report on principal developments in thin circular saw vibration and control research Part 1: Vibration of circular saws, Holz als Roh- und Werkstoff, 35 (1977) 189-196.

[2] K. Ono, T. Maeno, Theoretical and experimental investigation on dynamic characteristics of a 3.5-Inch flexible disk due to a point contact head, Tribology and Mechanics of Magnetic Storage Systems, 3 SP.21 (STLE) (1987) 144-151.

[3] M. Capino, The effect of initial curvature in a flexible disk rotating near a flat plate, ASME Journal of Tribology, 113 (1991) 355-360.

[4] R.C. Benson, K.A. Cole, Transverse “runout” of a nonflat spinning disk, Tribology Transaction, 34 (1991) 545-552.

[5] H.S. Jia, Analysis of transverse runout in rotating flexible disks by using Galerkin’s method, International Journal of Mechanical Sciences, 42 (2000) 237-248.

[6] J.-S. Chen, C.-C. Lin, Axisymmetrical snapping of a spinning non-flat disk, ASME Journal of Applied Mechanics, 72 (2005) 979-986.

[7] J.-S. Chen, T.-M. Huang, Deformation and Reverse Snapping of a Circular Shallow Shell under Uniform Edge Tension, International Journal of Solids and Structures, 43 (2006) 7776-7792.

[8] N.-C. Huang, Unsymmetrical buckling of thin shallow spherical shells, ASME Journal of Applied Mechanics, 30 (1964) 447-457.

[9] G.S. Schajer, North American techniques for circular saw tensioning and leveling: Practical measurement methods, Holz als Roh- und Werkstoff, 50 (1992) 111-116.

[10] J.L. Nowinski, Nonlinear transverse vibrations of a spinning disk, ASME Journal of Applied Mechanics, 31 (1964) 72-78.

[11] Y.-Y. Chang, On the deformation and reverse snapping speed of a spinning disk with unsymmetrical initial shape, Master Thesis, Department of Mechanical Engineering, National Taiwan University (2005).

Appendix: **Derivation of boundary conditions (20) and (21)**

To derive boundary conditions (20) and (21), we start with the definitions of strains and stress resultants (with dimensions) in Eqs. (3)-(11) to write the following relations:

$$u_{r,r} = \frac{1}{hE}\left(r^{-1}\phi_{,r} + r^{-2}\phi_{,\theta\theta} - \nu\phi_{,rr} - \frac{1-\nu}{2}\rho h\Omega^2 r^2 \right) - \frac{1}{2}\left(w_{,r}\right)^2 - \frac{1}{2}\left(w_{0,r}\right)^2 \tag{A1}$$

$$r^{-1}u_r + r^{-1}u_{\theta,\theta} = \frac{1}{hE}\left(\phi_{,rr} - \nu r^{-1}\phi_{,r} - \nu r^{-2}\phi_{,\theta\theta} - \frac{1-\nu}{2}\rho h\Omega^2 r^2 \right) - \frac{1}{2}r^{-2}\left(w_{,\theta}\right)^2 + \frac{1}{2}r^{-2}\left(w_{0,\theta}\right)^2 \tag{A2}$$

$$r^{-1}u_{r,\theta} + u_{\theta,r} - r^{-1}u_\theta = -\frac{2(1+\nu)}{hE}\left(r^{-1}\phi_{,\theta}\right)_{,r} - r^{-1}w_{,r}w_{,\theta} + r^{-1}w_{0,r}w_{0,\theta} \tag{A3}$$

At the inner radius $r = a$, u_r=0 and u_θ=0. Furthermore, due to the circular clamp at $r = a$ we have $u_{r,\theta}$=0 and $u_{\theta,\theta}$=0. We also assume that the initial shape w_0 satisfies the conditions $w_{0,r} = w_{0,\theta} = 0$ at the inner clamp. After deformation, the transverse displacement w satisfies the conditions $w_{,r} = w_{,\theta} = 0$ at the inner clamp. It then follows from Eq. (A2) that

$$\phi_{,rr} - \nu r^{-1}\phi_{,r} - \nu r^{-2}\phi_{,\theta\theta} = \frac{1-\nu}{2}\rho h\Omega^2 a^2 \tag{A4}$$

To derive the second boundary condition we first multiply Eq. (A2) by r, and differentiate it with respect to r. After using Eq. (A1) to eliminate $u_{r,r}$ we obtain

$$u_{\theta,r\theta} = \frac{1}{hE}[\phi_{,rr} + r\phi_{,rrr} + r^{-2}(\nu-1)\phi_{,\theta\theta} - \nu r^{-1}\phi_{,r\theta\theta} - r^{-1}\phi_{,r} - (1-\nu)\rho h\Omega^2 r^2] \tag{A5}$$

At this point we differentiate Eq. (A3) with respect to θ to obtain

$$r^{-1}u_{r,\theta\theta} + u_{\theta,r\theta} - r^{-1}u_{\theta,\theta} = -\frac{2(1+\nu)}{hE}\left(r^{-1}\phi_{,\theta\theta}\right)_{,r} \tag{A6}$$

By further assuming that $u_{r,\theta\theta} = 0$ at $r = a$, and comparing Eqs. (A5) and (A6) we obtain

$$r\phi_{,rrr} + (\nu-1)r^{-1}\phi_{,r} + (\nu+2)r^{-1}\phi_{,r\theta\theta} - 3r^{-2}\phi_{,\theta\theta} = \frac{1-\nu}{2}\rho h\Omega^2 a^2 \tag{A7}$$

After invoking the nondimensionalization schemes in Eq. (13), the two boundary conditions (A4) and (A7) can be nondimensionalized to the forms (after dropping the superposed asterisks) in Eqs. (20) and (21), respectively. In the special case when the

disk is flat and not rotating, Eqs. (A4) and (A7) return to the equations derived first by Huang [8] in 1964.

Tables

	P_0^1	P_0^2	P_0^3	P_{01}^1	P_{01}^{1*}
c_{00}	0	6.20	9.60	7.76	7.76
$c_{01(c)}$	0	0	0	3.37	-3.37

Table 1 Coordinates of the five equilibrium positions of an axisymmetrical disk with H_0=5 when $\Omega = 0$.

	$P_{01_c}^1$	$P_{01_c}^2$	$P_{01_c}^3$	$P_{01_c}^4$	$P_{01_c}^5$	$P_{01_{cs}}^1$	$P_{01_{cs}}^2$
c_{00}	0	7.50	5.96	9.74	5.94	7.33	7.33
c_{10}	0	-0.71	-0.83	-0.12	-0.08	-0.30	-0.30
$c_{01(c)}$	0	0.61	-2.96	-3.40	-6.97	-3.97	-3.97
$c_{01(s)}$	0	0	0	0	0	-3.81	3.81
$c_{11(c)}$	0	-0.49	-0.50	-0.14	-0.34	-0.29	-0.29
$c_{11(s)}$	0	0	0	0	0	-0.03	0.03
$c_{21(c)}$	0	0	-0.06	-0.02	-0.06	-0.04	-0.04
$c_{21(s)}$	0	0	0	0	0	-0.03	0.03
$c_{02(c)}$	0	0.01	0.02	0.03	0.12	0.12	0.12
$c_{02(s)}$	0	0	0	0	0	0	0
$c_{12(c)}$	0	-0.05	0.02	0.03	0.11	0.21	0.21
$c_{12(s)}$	0	0	0	0	0	-0.11	0.11

Table 2 Coordinates of the seven equilibrium positions of an unsymmetrical disk with H_0=5 and H_1=3 when $\Omega = 0$.

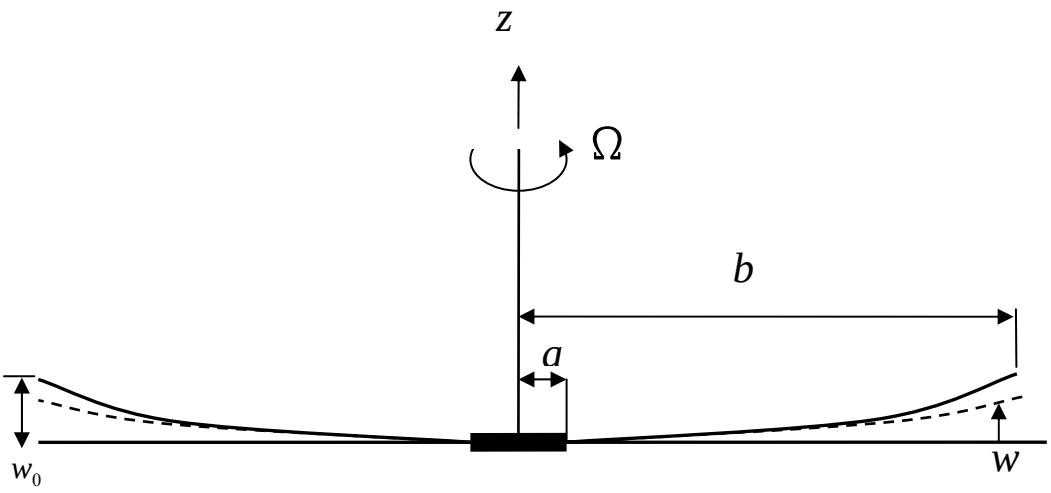

Figure 1 A spinning non-flat disk.

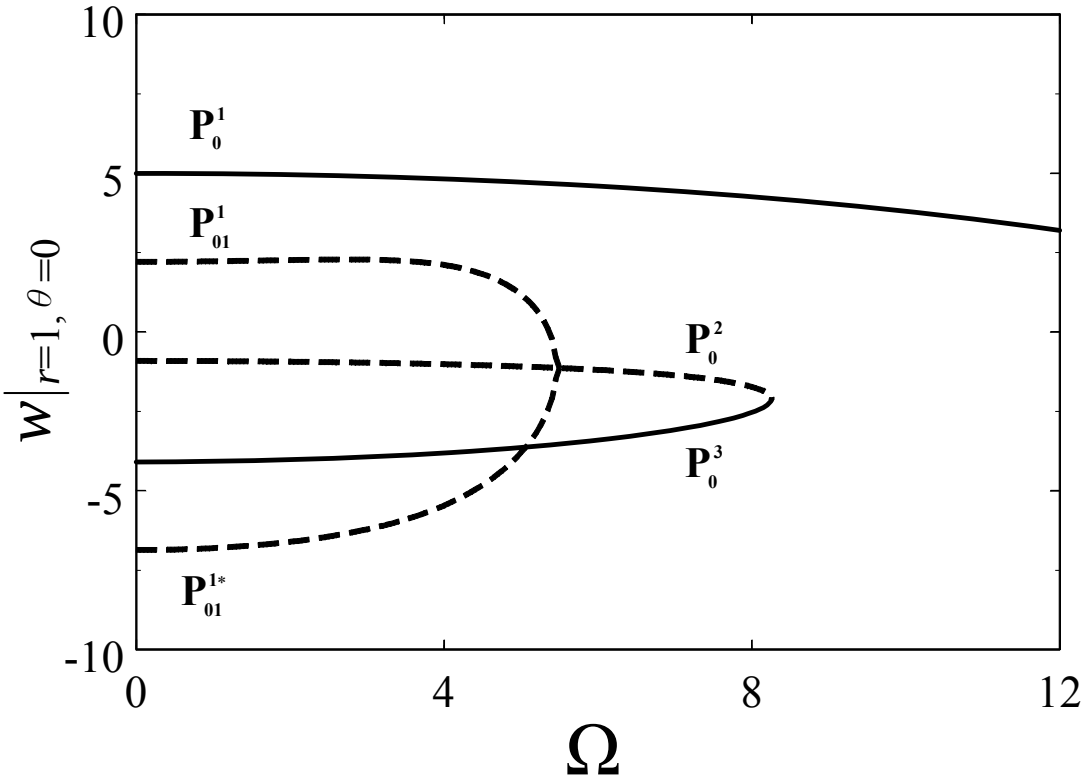

Figure 2 Disk position as a function of the rotation speed for an axisymmetrical disk with H_0=5.

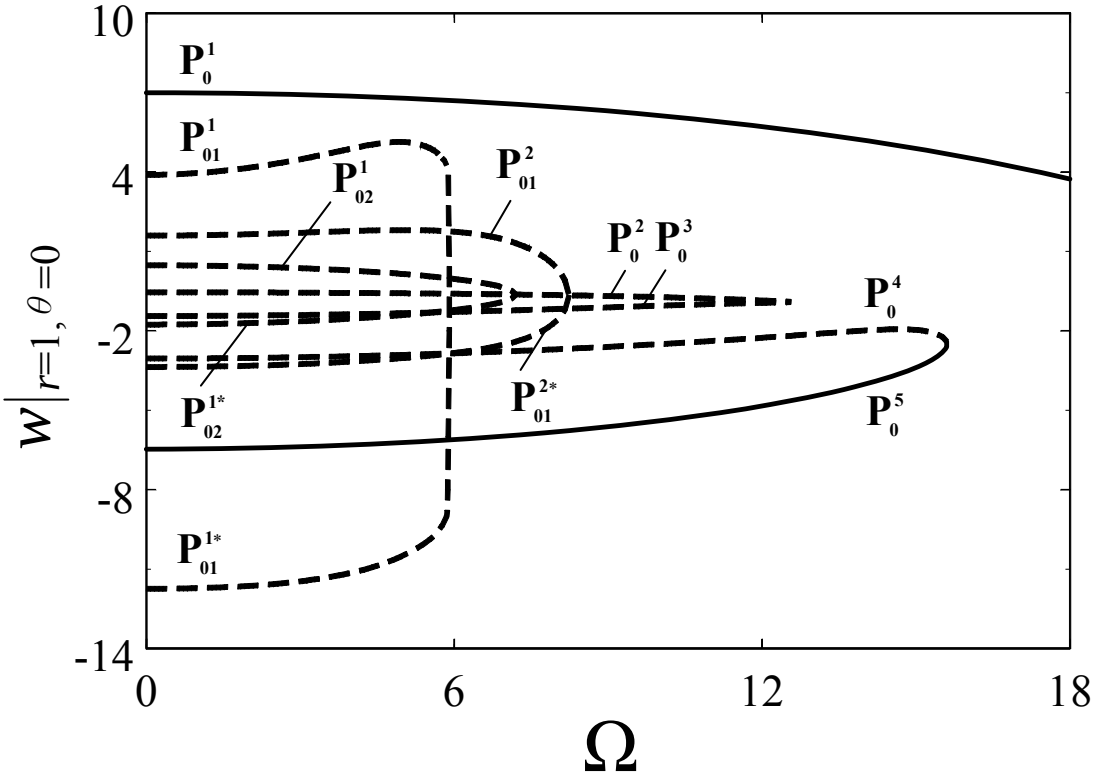

Figure 3 Disk position as a function of the rotation speed for an axisymmetrical disk with H_0=7.

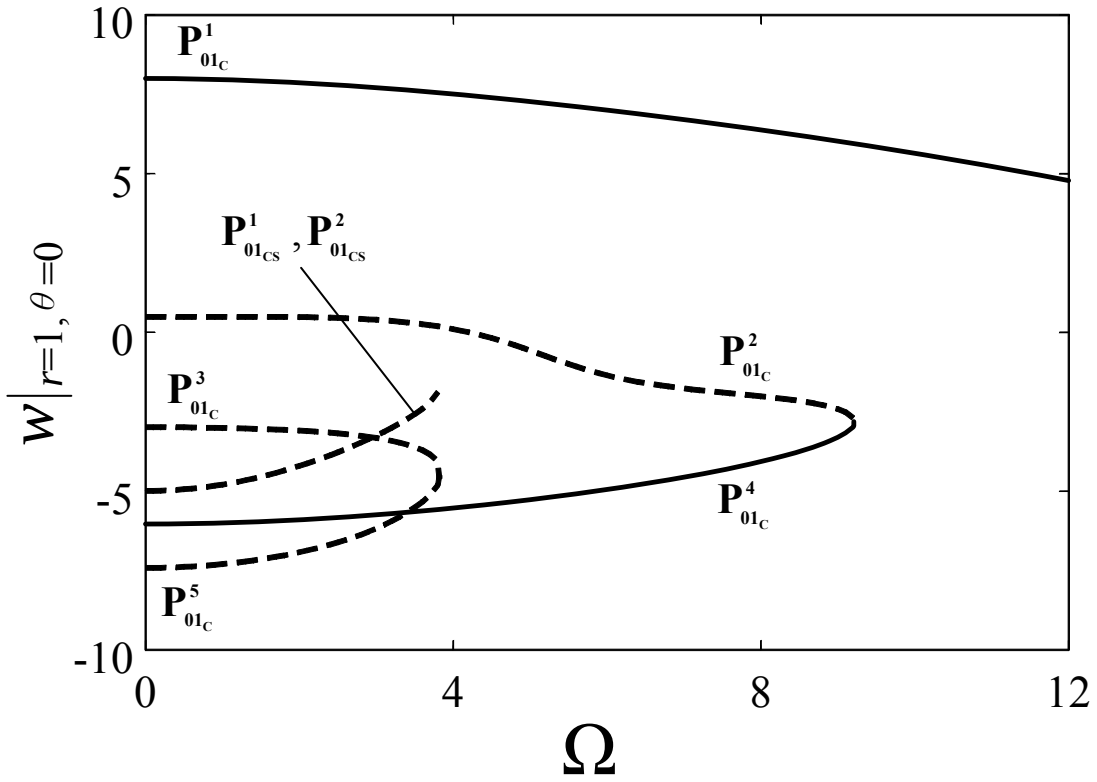

Figure 4 Disk position as a function of the rotation speed for an unsymmetrical disk with H_0=5 and H_1=3.

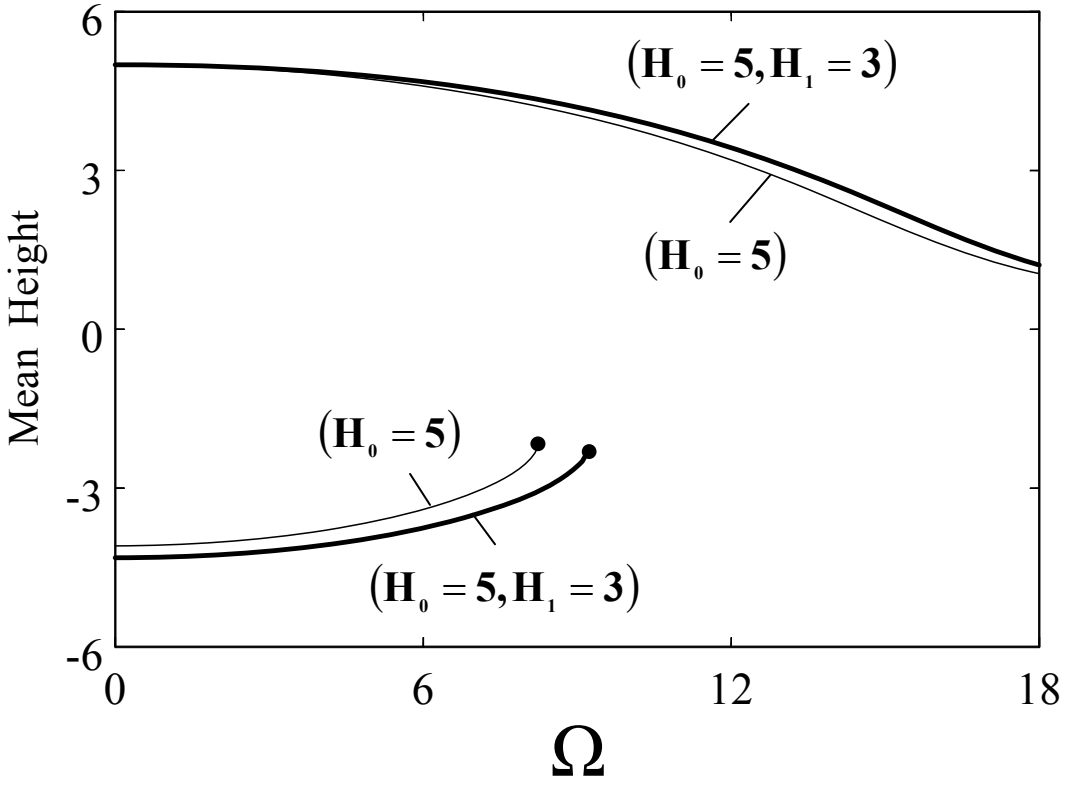

Figure 5 Mean heights of the two stable solutions on the outer rim. Thick lines are for the unsymmetrical disk with H_0=5 and H_1=3. Thin lines are for the axisymmetrical disk with H_0=5.

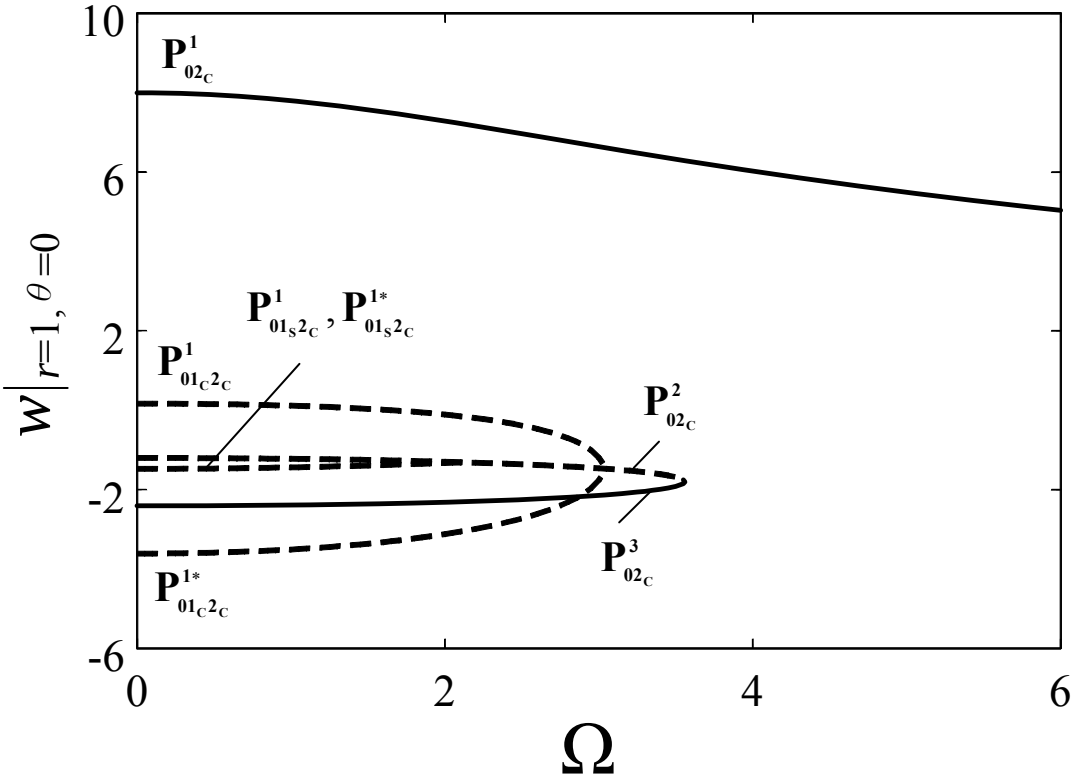

Figure 6 Disk position as a function of the rotation speed for an unsymmetrical disk with H_0=5 and H_2=3.

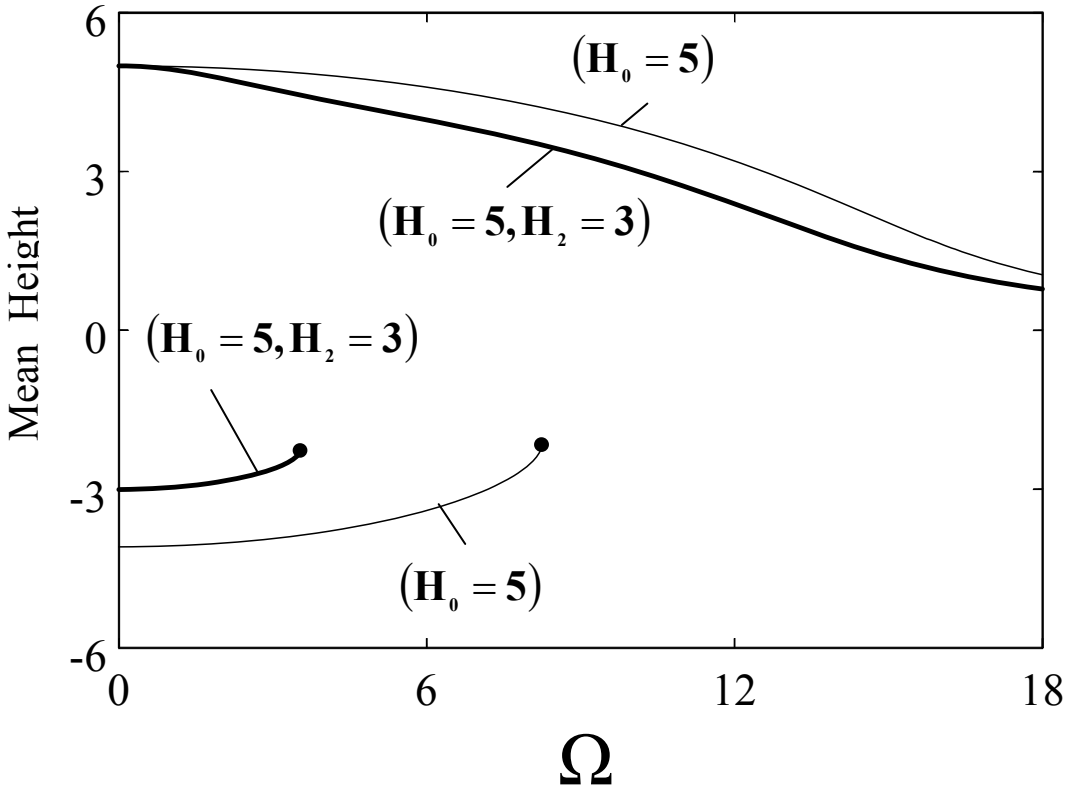

Figure 7 Mean heights of the two stable solutions on the outer rim. Thick lines are for the unsymmetrical disk with H_0=5 and H_2=3. Thin lines are for the axisymmetrical disk with H_0=5.

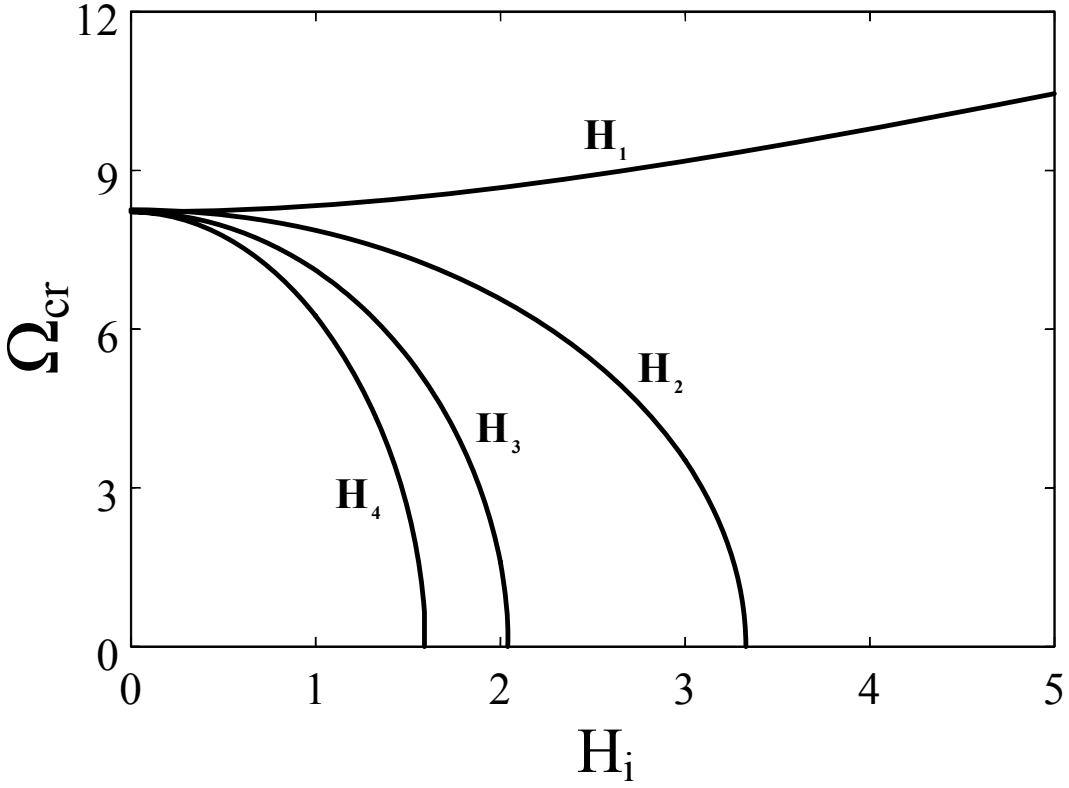

Figure 8 Relation between the reverse snapping speed Ω_{cr} and various unsymmetrical components H_i with $i \geq 1$. The axisymmetrical component H_0 is fixed at 5.

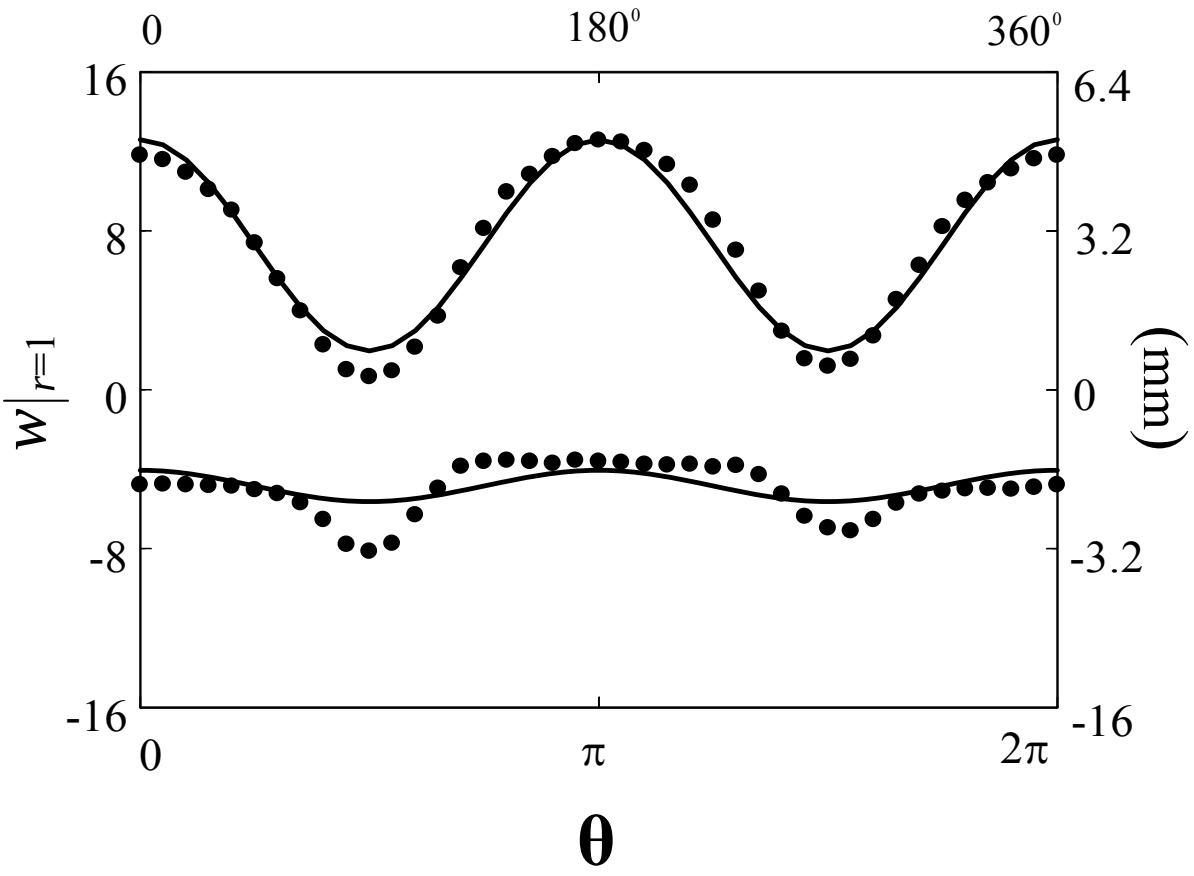

Figure 9 The symbol • represents the measured height relative to the clamping plane at various points on the outer rim for both the unstressed (upper) and stressed (lower) positions when the disk is not rotating. Solid lines are theoretical predictions.

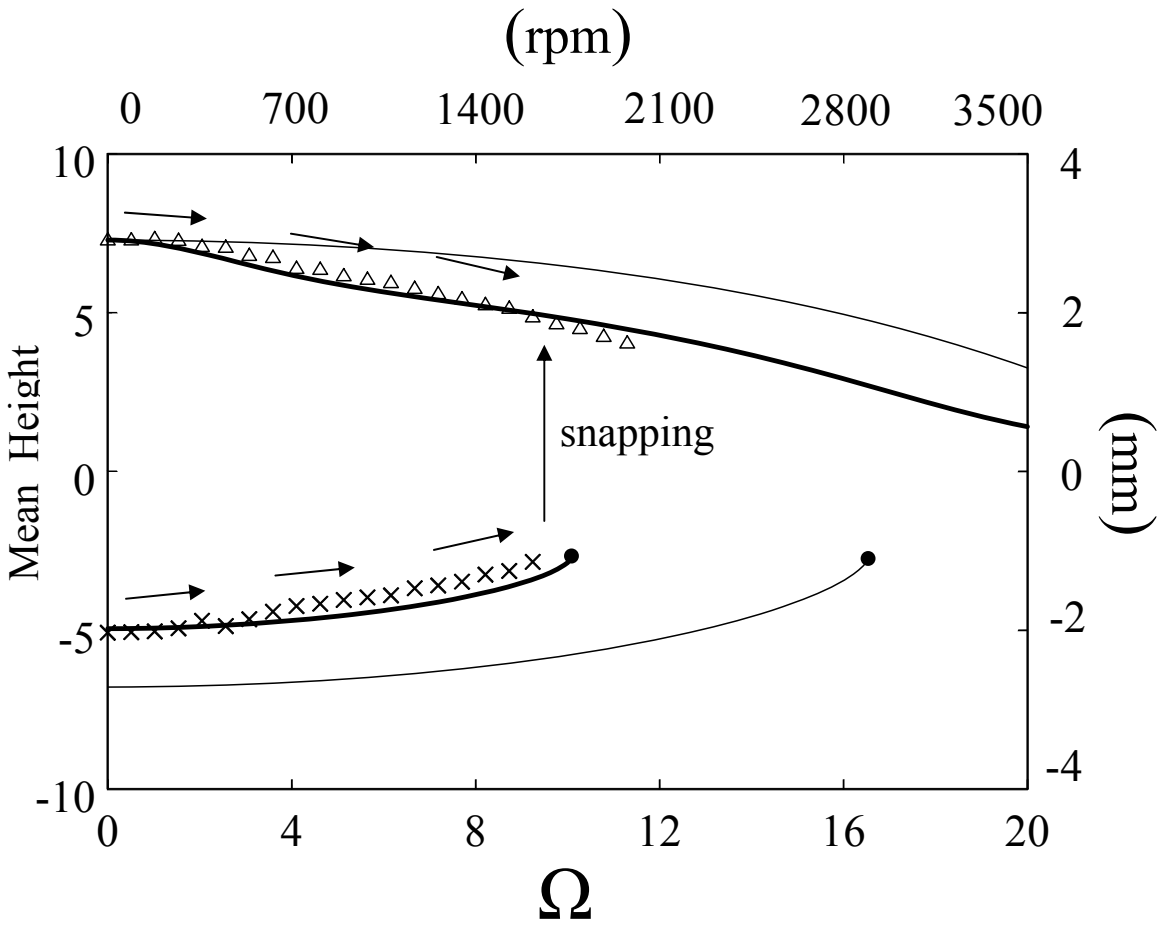

Figure 10 Measurement of disk mean height at the outer rim as a function of rotation speed. Thick and thin lines are theoretical predictions based on the unsymmetrical and axisymmetrical theories, respectively

計畫成果自評:

This project has been conducted in a very effective manner. All the goals listed in the proposal are accomplished. The academic value of this report is confirmed from the acceptance of this manuscript by International Journal of Non-Linear Mechanics with high regard.